Materials Science Forum
ISSN: 1662-9752, Vol. 1183, pp 81-92
doi:10.4028/p-5wea0U

Submitted: 2026-01-19
Revised: 2026-02-24
Accepted: 2026-02-25
Online: 2026-04-13

Extension of the Lemaitre Damage Model to Account for Static and Dynamic Recrystallization Behavior

Moritz Gouverneur[1,a*], David Bailly[1,b] and Junhe Lian[1,c]

[1]Institut of Metal Forming, RWTH Aachen University; Intzestraße 10, 52072 Aachen, Germany

[a*]moritz.gouverneur@ibf.rwth-aachen.de, [b]david.bailly@ibf.rwth-aachen.de, [c]junhe.lian@ibf.rwth-aachen.de

Keywords: forging, damage, modelling, simulation.

Abstract. Open-die forging is an incremental bulk metal forming process for producing large, safety-relevant components such as turbine and generator shafts. Besides achieving the target geometry, the process improves mechanical properties through grain refinement and the elimination of casting-related defects. With the increasing use of high-alloy steels, precise process control is required to prevent surface and internal cracking caused by material damage. However, predictive models for damage evolution under the thermo-mechanical conditions of open-die forging remain limited, particularly with respect to high-temperature recrystallization and the incremental process character with inherent pause times. In this work, a recrystallization-sensitive damage model was developed and validated for open-die forging. The parameters of the Lemaitre damage formulation were determined for the cold work tool steel D2 (1.2379, X155CrVMo12-1) using hot tensile tests over the relevant forging temperature range. Dynamic recrystallization kinetics were characterized by hot compression tests and described using an Avrami-type JMAK formulation, while static recrystallization behavior was analyzed by stress relaxation experiments and also modeled with JMAK kinetics. These results enabled the quantification of recrystallized fractions as functions of strain, temperature, strain rate, and dwell time. To link microstructural evolution with damage development, tailored recrystallization states were generated in dilatometer experiments and examined metallographically with respect to void formation and healing. The extended model was implemented in a finite element framework and validated through open-die forging experiments on demonstrator geometries, showing its capability to predict damage initiation under industrially relevant conditions.

Introduction

Open-die forging is an incremental bulk metal forming process that enables the manufacturing of longitudinally oriented components with various cross-sections like shafts as well as more complex shaped components like bushings.

In this process, the workpiece is heated to forging temperature, positioned beneath the press by a manipulator, and plastically deformed in a stroke-wise manner using tools of simple geometry, such as flat or slightly contoured dies. By the targeted execution of often several hundred individual strokes over multiple passes and forging heats, the final component geometry is achieved. While forging, the goal is not only to achieve a specific geometry, but also to achieve excellent material properties. This is possible due to the ability to close casting related voids and to convert coarse microstructure resulting from casting in a fine homogeneous one [1].

The increasing demand for open-die forged components made from highly developed and alloyed steels necessitates increasingly precise and reproducible process control, in particular with respect to narrow allowable temperature and forming windows. In industrial practice, however, open-die forging operations are still frequently performed under manual control. This leads to unavoidable process fluctuations, for example in temperature management, positioning accuracy, and height reduction per pass, which significantly increase the risk of exceeding critical process limits and promote the formation of surface and internal cracks.

To compensate for these uncertainties, forged components are often produced with increased oversize. While this approach improves process robustness, it results in substantially higher material consumption. Given that the starting material can account for more than 50% of the total manufacturing cost of forged components [2], oversizing leads to increased production costs, higher energy demand, and elevated CO_2 emissions [3,4]. This contradicts the efforts to minimize material usage and machining through near-net-shape production. Furthermore, approaches known to reduce the risk of cracking, such as applying smaller height reductions per pass or introducing additional reheating steps, are also commonly employed in practice. Although these measures reduce local strain accumulation and thermal gradients, they significantly increase forging time, energy consumption, and overall production costs. Consequently, such approaches are not economically viable for the efficient production of large or complex forged components.

To analyze the risk of cracking and to assess the suitability of alternative process routes, various damage models were developed in the past. However, application in open-die forging is usually difficult because most approaches were originally developed for other types of loading, e.g. sheet metal forming [5], or they do not account to changing load directions like in incremental forming processes [6]. In addition, the approaches are often designed for cold forming, meaning that they do not consider softening mechanisms such as recovery and recrystallisation [7].

Based on these considerations, this work focuses on the calibration and extension of the damage model of effective stresses originally proposed by Lemaitre [8]. Building upon the approach introduced by Rüf et al. [9], the model is adapted for application in open-die forging, as the stress states encountered in warm upsetting processes show strong similarities to those occurring during incremental forging operations. In a first step, the damage model is calibrated using hot tensile tests conducted up to material failure. To enhance the predictive capability of the model under hot forging conditions, the formulation is subsequently extended to incorporate the influence of dynamic recrystallization, which is known to reduce damage during high-temperature deformation [10]. Furthermore, to account for the incremental nature of open-die forging and the associated dwell times between forming steps, the behavior and impact of static recrystallization are experimentally characterized and integrated into the damage formulation. Finally, the extended model is applied within a finite element framework to analyze damage evolution in a representative open-die forging process.

Damage Modeling

In metal forming processes, material formability is fundamentally limited by the initiation and evolution of damage, ultimately leading to failure. In this context, damage is defined as the nucleation of microvoids and microcracks, as well as their subsequent growth and coalescence during deformation. Progressive damage accumulation eventually results in the formation of macroscopic cracks, which corresponds to the failure of the formed component [11].

For the damage-minimized design and assessment of open-die forging processes, it is essential to reliably predict the evolution of material damage as a function of process parameters. This includes not only the spatial distribution and magnitude of damage but also the initiation of macroscopic cracking with sufficient accuracy. To do so, numerous approaches for describing damage and failure are available in the literature. Most of these approaches are based on stress- and strain-dependent functions, which can be obtained from continuum mechanical descriptions but cannot be directly measured during the forming process. Here, damage models can generally be classified into history-independent and history-dependent formulations. History-independent approaches evaluate damage solely based on the current stress or strain state and are therefore mainly suitable for simplified limit assessments [12,13]. In contrast, history-dependent approaches consider the forming history and thus enable a more accurate description of damage evolution [14,15]. A further distinction can be made between macromechanical and micromechanical damage models, depending on the type of variables used to describe material damage. Macromechanical models rely on global variables, whereas micromechanical models consider local stress and strain states.

Due to the incremental character of open-die forging, the complex thermo-mechanical boundary conditions, and frequently changing loading directions, the local stress and strain states can vary significantly throughout the workpiece volume. Consequently, history-dependent, micromechanically motivated damage models are particularly well suited for the simulation of open-die forging processes, as they inherently consider both the complete forming history and the local stress state in the evaluation of material damage. Recent publications on damage modeling in metal forming emphasize the importance of such approaches, especially when aiming at predictive simulations under hot forming conditions and in combination with microstructure evolution [7,11,14-17].

Model of effective stresses.

To describe ductile material damage, Lemaitre introduced the forming history-dependent and micromechanically motivated Model of Effective Stresses (MES) [2]. The MES represents a compromise between computational efficiency, practical applicability in terms of parameter calibration, and the number of required input variables. By considering a representative volume element (RVE), the model assumes that, in the presence of material damage D, only the undamaged surface fraction $(1-D)$ of a sectional plane within the RVE is capable of transmitting forces.
For the one-dimensional case, the effective stress $\tilde{\sigma}_{eff}$ is defined as:

$$\tilde{\sigma}_{eff} = \frac{F}{A} = \frac{F}{A_0 - A_D} = \frac{\sigma}{1-D}. \tag{1}$$

Here F denotes the normal force, A_0 the total cross-sectional area, and A_D the area fraction occupied by voids due to damage. Accordingly, the damage variable is defined as $D = A_D/A_0$ where D=0 describes an undamaged and D=1 describes a failed material state. Assuming isotropic damage, the effective Cauchy stress tensor $\tilde{\sigma}_{ij}$ is given by:

$$\tilde{\sigma}_{ij} = \frac{\sigma_{ij}}{1-D}. \tag{2}$$

The evolution of damage is described by Lemaitre through the dissipation potential ψ, resulting in a scalar, convex damage evolution law:

$$\dot{D} = \frac{\partial \psi}{\partial Y} = \left(\frac{Y}{S_0}\right)^{s_0} \cdot \dot{\bar{\varepsilon}}. \tag{3}$$

In this law S_0 is a material parameter, $\dot{\bar{\varepsilon}}$ is the equivalent plastic strain rate, and Y denotes the damage energy release rate. The parameter s_0 is a material-specific calibration factor controlling damage sensitivity. As no significant influence of s_0 on the model calibration was observed, it was set to $s_0 = 1$. To distinguish between tensile and compressive stress states, the stress tensor is decomposed into positive and negative components, yielding in the following description for the energy release rate:

$$Y = \frac{1+\nu}{2 \cdot E} \cdot \left[\frac{\langle\bar{\sigma}\rangle : \langle\bar{\sigma}\rangle}{(1-D)^2} + \frac{h \cdot \langle -\bar{\sigma}\rangle : \langle -\bar{\sigma}\rangle}{(1-h \cdot D)^2}\right] - \frac{\nu}{E} \cdot \left[\left(\frac{tr(\langle\bar{\sigma}\rangle)}{1-D}\right)^2 + h \cdot \left(\frac{tr(\langle -\bar{\sigma}\rangle)}{1-h \cdot D}\right)^2\right]. \tag{4}$$

Here ν is the Poisson's ratio, E the Young's modulus, $\bar{\sigma}$ the true stress tensor, and h a void-closure parameter accounting for the potential reduction of damage under compressive loading. For an accurate representation of damage evolution, h should be close to zero. By comparing simulations with tensile and compression tests, Rüf [9] showed that h should therefore be set to 0.001.
According to Lemaitre, the material parameter S_0 can be approximated by

$$S_0 = \frac{\sigma^2}{2 \cdot E \cdot (1-D)^2 \cdot \frac{dD}{d\varepsilon}} \approx \frac{\sigma_r^2}{2 \cdot E \cdot (1-D)^2 \cdot \frac{D_{1c}}{\varepsilon_r}} \tag{5}$$

where σ_{eq} is the equivalent stress, D_{1c} the critical damage under uniaxial tension, and ε_r the elongation at rupture under uniaxial tension. The one-dimensional critical damage and the general rupture criterion D_c are defined as:

$$D_{1c} = 1 - \frac{\sigma_r}{\sigma_u}. \qquad D_c = D_{1c} \cdot \frac{\sigma_u^2}{\sigma_{eq}^2 \cdot \tau_x} \tag{6}$$

Here σ_u is the ultimate tensile strength, σ_r the failure stress, and $\tau_x$the stress triaxiality function [18]. To describe the damage evolution over time (time increment Δt) the incremental description in Eq. 7 is used:

$$D_i = D_{i-1} + \frac{\dot{D} \cdot \Delta t}{D_c}. \tag{7}$$

To identify the material parameters required for the MES damage model, hot tensile tests were conducted at IBF using a TA DIL805 quenching and forming dilatometer. Flat tensile specimens of tool steel X155CrVMo12-1 with a thickness of 2.2 mm and a width of 3 mm in the formed section were used. The specimens were inductively heated to the forming temperature and deformed at a constant strain rate of 0.1 s^{-1} until fracture. The quenching and forming dilatometer enables experiments under vacuum conditions while providing highly precise and reproducible temperature control throughout the test. The experiments were carried out for typical forging temperatures in a temperature range from 800 to 1200 °C. To ensure reproducibility, each test was performed twice.
The resulting mean values of ultimate tensile strength σ_u, failure stress σ_r, and rupture elongation ε_r, together with the corresponding damage resistance parameter S_0 evaluated for each temperature according to Eq. 5 and 6, are summarized in Table 1. Based on these experimentally determined material properties and the derived S_0-values, the MES damage model is fully calibrated for the tool steel X155CrVMo12-1. Within the investigated temperature range, the temperature-dependent parameters are obtained by interpolation between the tabulated values.

Table 1. Results of the warm tensile tests of the tool steel X155CrVMo12-1.

Temperature [°C]	Ult. tensile strength σ_u [MPa]	Failure stress σ_r [MPa]	Rupture elongation ε_r [%]	Parameter S_0 [-]
800	170.9	67.9	38.5	0.071
900	121.6	132.3	30.8	0.060
1000	143.1	66.2	34.4	0.076
1100	98.5	32.8	35.7	0.041
1200	62.0	16.5	36.0	0.021

Modeling of DRX Kinetics.

In materials exhibiting low stacking fault energy, such as the cold work tool steel X155CrVMo12-1 investigated in this study, microstructural softening during hot deformation is governed predominantly by recrystallization mechanisms rather than by recovery effects [19]. Recrystallization processes occurring concurrently with plastic deformation are referred as (meta) dynamic recrystallization (DRX), in contrast to static recrystallization (SRX), which takes place during post-deformation holding periods. At the same time, previous investigations have demonstrated that recrystallization contributes to a reduction in material damage during hot forming by effectively resetting critical strain levels and promoting the closure of small voids [10]. Consequently, the incorporation of DRX effects is of particular importance for physically motivated damage modeling in hot forming processes such as open-die forging.

As the MES was originally formulated for cold forming applications and does not account for microstructural softening phenomena, it was extended to incorporate the influence of DRX, following the general approach proposed in [9]. For this purpose, the kinetics of dynamic recrystallization were experimentally determined for the tool steel X155CrVMo12-1 using cylindrical Rastegaev specimens with an initial diameter of 10 mm and a height of 15 mm. The tests were carried out on a Servotest TMTS servo-hydraulic testing machine at strain rates of 0.1 s^{-1} and 1 s^{-1} for temperatures of 800 °C, 900 °C, 1000 °C, 1100 °C, and 1200 °C, with each thermo-mechanical condition being tested twice. Based on the resulting flow curves, the evolution of the dynamically recrystallized fraction was evaluated in accordance with the methodology proposed by Sun et al. [20] and Brüggemann et al.

[21]. For this purpose, the flow curves determined are divided into a portion subject only to recovery (DRV) and a portion softened due to dynamic recrystallization (DRX). Fig. 1 exemplarily illustrates the procedure for a flow curve at 900 °C and a strain rate of 0.1 s^{-1}.

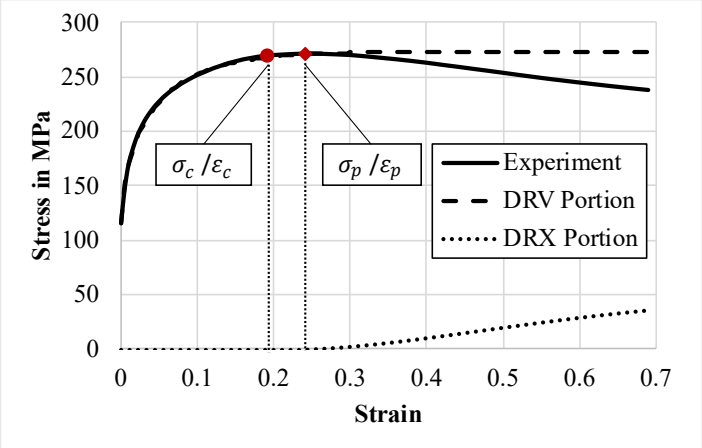

Fig. 1. Exemplary determination of the dynamically recrystallized fraction (DRX) according to Sun et al. [20] at a temperature of 900°C and a strain rate of 0.1 s^{-1}.

For each test, the peak stress σ_p and the corresponding strain ε_p were first determined from the experimental flow curve. The critical strain for the onset of DRX ε_c was then estimated by assuming $\varepsilon_c = 0.8 \cdot \varepsilon_p$, as indicated in Fig. 1. The dependence of ε_c on temperature and strain rate over the investigated range was subsequently described as a function of the Zener–Hollomon parameter Z in accordance with Eq. 8.

$$\varepsilon_c = c_1 \cdot Z^{c_2} \quad \text{with} \quad Z = \dot{\varepsilon} \cdot exp\left(\frac{Q_w}{R \cdot T}\right) \tag{8}$$

The DRV portion of the flow curve was obtained by extrapolating the work-hardening behavior of the experimental flow curve beyond the critical strain ε_c. The DRX portion was then evaluated from the difference between the measured flow curve and the DRV curve, yielding the strain-dependent dynamic recrystallized fraction $X_{\mathrm{DRX}}(\varepsilon)$. The DRX fractions from all tests, covering all investigated temperatures and strain rates, were finally analyzed in conjunction. The fraction of dynamically recrystallized material X_{DRX} is described by Eq. 9, where the material specific parameters n and k were identified by non-linear least-squares fitting of X_{DRX}.

$$X_{DRX} = 1 - exp\left(-k \cdot \left(\frac{\varepsilon - \varepsilon_c}{\varepsilon_c}\right)^n\right) \tag{9}$$

The material-specific parameters describing the DRX kinetics of X155CrVMo12-1 within the investigated temperature and strain rate range are summarized in Table 2.

Table 2. Determined material parameters of DRX kinetics for the tool steel X155CrVMo12-1.

Activation energy Q_w $[kJ/mol]$	Parameter k [-]	Parameter n [-]	Parameter c_1 [-]	Parameter c_2 [-]
232.212	0.47077	2.094	0.179	0.0093

Modeling of SRX Kinetics.

Due to the incremental nature of open-die forging and the associated frequent dwell times between the forming steps at elevated temperatures during every pass, the microstructure kinetics of the process are also strongly driven by static effects. To account for the influence of those static recrystallization effects during these pause times, the SRX kinetics were determined by means of stress relaxation experiment.

Therefore, additional hot compression tests were carried out on cylindrical specimens of X155CrVMo12-1 with an initial diameter of 5 mm and a height of 10 mm using the IBF quenching

and forming dilatometer TA DIL 805. The compression tests were conducted at 800 °C, 900 °C, 1000 °C, 1100 °C and 1200 °C with different height reductions representing true strains of 0.10, 0.125, and 0.15 in the sample. The applied height reduction was selected for each temperature such that the imposed strain remained below the previously determined critical strain, ensuring that no dynamic recrystallization effects occurred. After reaching the desired deformation, the compression stroke was held constant and the resulting stress relaxation was measured. Based on the obtained stress relaxation curves, the SRX kinetics were subsequently determined as a function of temperature and applied strain according to Karjalainen [22]. For this purpose, the stress relaxation curves were divided into three distinct regions (see Fig. 2): In region 1, creep processes initially dominate the stress relaxation behavior. This is followed by region 2, in which SRX takes place. After completion of SRX, recovery processes are observed in region 3.

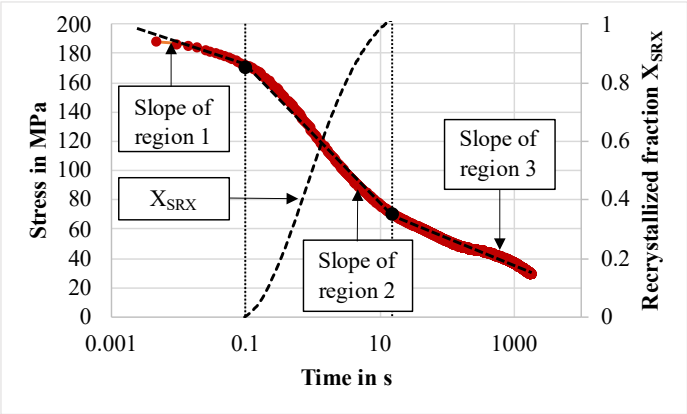

Fig. 2. Stress relaxation curve with three characteristic regions and static recrystallized fraction at 1000 °C.

By fitting linear functions to regions 1 and 3 in the $\log(t)$–stress representation the stresses of the purely unrecrystallized and fully recrystallized states are obtained. The respective parameters describing the linear functions are given by the y-axis intercept σ_0 and the slope α with indices 1 for the first and 2 for the third region of stress relaxation. The statically recrystallized fraction X at any time within region 2 is then determined individually for each temperature and forming condition using a linear mixture rule based on the measured stress σ:

$$X = \frac{(\sigma_{01} - \alpha_1 \cdot log(t)) - \sigma}{(\sigma_{01} - \sigma_{02}) - (\alpha_1 - \alpha_2) \cdot log(t)} \tag{10}$$

For each temperature and strain level, the resulting statically recrystallized fraction X were subsequently fitted with the JMAK-type relation given in Eq. 11, providing an individual description of the SRX kinetics in terms of the Avrami exponent n and the half-life time t_{50}, which is defined as the time required for 50 % static recrystallization.

$$X_{SRX} = 1 - exp\left(\ln(0.5) \cdot \left(\frac{t}{t_{50}}\right)^n\right) \tag{11}$$

To enable a generalized description of SRX kinetics over a broad range of thermo-mechanical conditions, the experimentally determined Avrami exponents were averaged. The temperature and strain dependence of the half-life time $t_{50}$was described using Eq. 12 [23]:

$$t_{50} = A \cdot \varepsilon^q \cdot exp\left(\frac{Q}{R \cdot T}\right) \tag{12}$$

The activation energy $Q$and the material-specific parameters A and q in Eq. 12 were obtained from logarithmic plots of the half-life time as a function of temperature and strain by linear fitting using a non-linear least-squares procedure. The corresponding parameter values are summarized in Table 3.

Table 3. Determined material parameters of SRX kinetics for the tool steel X155CrVMo12-1.

Activation energy Q $[kJ/mol]$	Avrami exponent n [-]	Parameter A [-]	Parameter q [-]
114.010	0.5553	0.00002335	-0.7228

Damage development due to recrystallization effects.

Using the model parameters identified in the previous sections, the fractions of dynamically and statically recrystallized microstructure during open-die forging can be predicted for the tool steel X155CrVMo12-1. Nevertheless, a constitutive link between microstructural evolution and the development of material damage must be established.

The effect of dynamic recrystallization on damage evolution is incorporated using the formulation proposed by Abu Al-Rub et al. [24], which has also been employed in the work of Rüf et al. [9]. Unlike the original formulation, the present approach was extended to account for the dynamically recrystallized fraction in an incremental manner. As a result, the damage parameter defined in Eq. 7 is reformulated as a function of the dynamically recrystallized fraction ΔX_{DRX}:

$$D_i = D_{i-1} + \frac{\dot{D}\cdot\Delta t}{D_c}\cdot(1-\Delta X_{DRX}). \tag{13}$$

In contrast to dynamic recrystallization, no general constitutive approaches are available to describe the influence of static recrystallization on damage evolution. Consequently, an experimental strategy, based on the work of Heiser et al. [25], was employed. The objective of this methodology is to describe the evolution of material damage by means of the void area fraction as a function of the statically recrystallized fraction.

To this end, cylindrical tensile specimens of X155CrVMo12-1 with an initial diameter of 10 mm and a measure length of 50 mm were manufactured and tested at room temperature in accordance with DIN EN ISO 6892-1 [26] on a Zwick Z100 tensile testing machine up to uniform elongation. This procedure ensures that a sufficient and homogeneous pre-damage state is introduced into the specimens under tensile loading, enabling microscopic investigation of damage evolution. From the deformed sections of the tensile specimen, cylindrical compression samples with an initial diameter of 5 mm and a height of 10 mm were subsequently extracted. These specimens were subjected to single-step compression tests using the quenching and forming dilatometer TA DIL 805. The deformation parameters were selected according to the SRX kinetics determined in the previous section to achieve statically recrystallized fractions of 0%, 50%, and 95%. Table 4 provides an overview of the specific process parameters.

Table 4. Determined process parameters to archive defined statically recrystallized fractions.

Temperature $[°C]$	Holding time [s]		
	0% SRX	50% SRX	95% SRX
800	0	2.3	28.1
900	0	3.5	42
1000	0	4.9	59
1100	0	6.5	78.9

After deformation, the samples were sectioned in height, prepared metallographically and analyzed using a Keyence VHX-7000 digital microscope. High-resolution 4K imaging combined with advanced image processing enabled automated detection and quantification of voids based on brightness threshold. Fig. 3 shows an exemplary microscopic image of a dilatometer specimen with no statically recrystallized fraction.

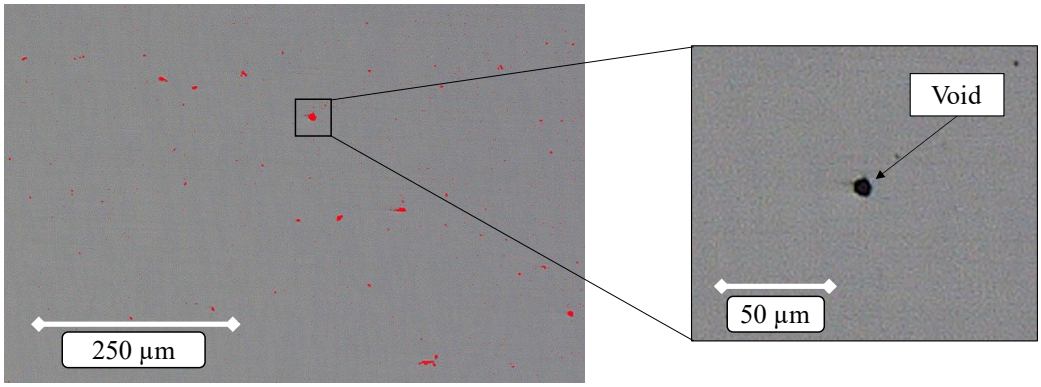

Fig. 3. Microscopic image of a formed sample. Left: Automatic void detection. Right: Close-up of a void.

Fig. 3, right shows that the voids are clearly visible as dark features in the microstructure. By applying a brightness threshold, voids can be automatically identified, marked, counted, and measured (see Fig. 3, left). For each specimen, a square evaluation area with an edge length of approx. 2500 µm was analyzed. The selection of a sufficiently large measurement area ensures that the determined void area fraction reflects the overall damage state of the material rather than local microstructural variations. Based on these analyses, the void area fraction was determined for all experiments. Fig. 4 summarizes the averaged void area fractions as a function of the statically recrystallized fraction, revealing a clear decrease in void area fraction with increasing static recrystallization.

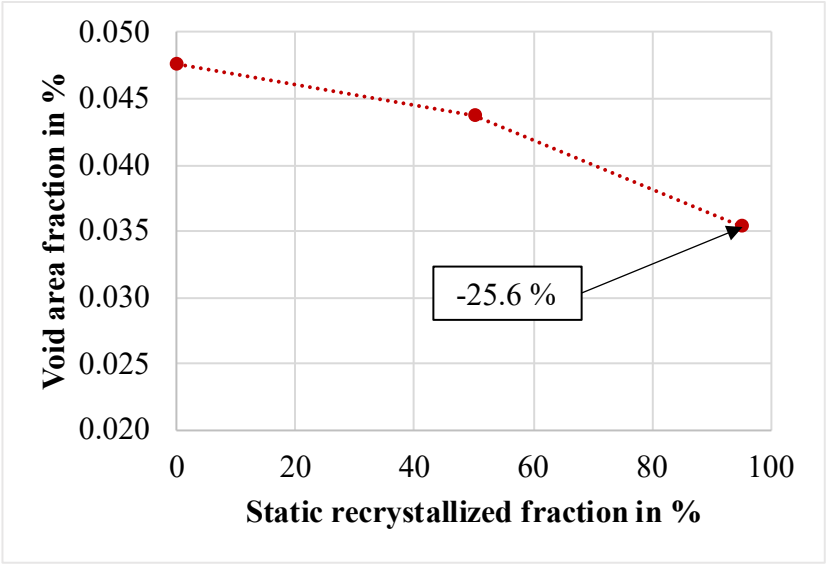

Fig. 4. Void area fraction as a function of the static recrystallized fraction.

Fig. 4 shows that the average void area fraction of approximately 0.048 % was reduced by m_{SRX} =25.6 % to about 0.035 % at near-complete static recrystallization.

These results confirm a direct relationship between the statically recrystallized microstructural fraction and the void area fraction, and thus material damage. With increasing statically recrystallized fraction, a significant healing of voids occurs, leading to a substantial decrease in the overall damage level. To account for this effect in the damage model, the damage variable D_i in Eq. 13 is reduced in the presence of static recrystallization according to the statically recrystallized fraction and the experimentally determined void reduction factor m_{SRX}. The resulting damage formulation including static recrystallization is given by:

$$D_{SRX,corr} = D_i + (1 - \Delta X_{SRX} \cdot m_{SRX}) \tag{14}$$

Experimental Validation

The conducted forging trials served to experimentally validate the calibrated and extended damage model. The objective was to forge a demonstrator component in which different damage states could be deliberately induced, including regions exhibiting pronounced cracking as well as regions showing no or only incipient cracks. In parallel, the identical forging process was simulated using the calibrated and extended damage model, enabling a direct comparison between experimental observations and numerical predictions.

The initial workpiece geometry was a rectangular block measuring 150 × 150 × 800 mm³, which was forged into a stepped rectangular shape with final cross-sections of 115 × 115 mm² and 95 × 95 mm². Forging was performed at 1200 °C using a relative height reduction of 15% and a bite ratio of 0.5. All strokes were applied without bite offset and in a purely feeding manner. The resulting forging plan is shown in Table 5.

Table 5. Forging plan for experimental validation.

Pass [-]	Height reduction [%]	Initial height [mm]	Final height [mm]	Bite length [mm]	Bite ratio [-]	Strokes [-]
1	15	150	128	75	0.5	7
2	14.5	157	135	79	0.5	7
3	15	135	114	67	0.5	9
4	14.5	141	121	71	0.5	10
5	7	121	112	60	0.5	13
6	6.8	123	115	62	0.5	13
7	15	115	98	58	0.5	5
8	14.5	121	103	60	0.5	6
9	11.6	103	91	52	0.5	7
10	11.3	107	95	54	0.5	8

The forging plan consists of ten passes executed within a single heat, with the first six passes applied over the full length of the block and the remaining four passes used to form the step over half the block length (see Fig. 5).

The experimental trials were conducted at the IBF forging facility, which combines a 630-ton hydraulic forging press with a six-axis hydraulic heavy-duty robot. This setup enables industrially relevant forming conditions as well as highly reproducible workpiece positioning. Ultrasonically tested blocks free of reportable defects according to EN 10228-4 [27] were used as starting material to exclude significant pre-damage. Prior to forging, the blocks were heated to forging temperature at 1200 °C in a gas furnace and held for 1.5 hours to ensure temperature homogeneity before being forged according to the defined forging plan. The forging was carried out using two flat dies with a width of 200 mm and a radius of 20 mm. During forging, the heavy-duty robot and the forging press operated in automatic mode, ensuring high repeat accuracy of the strokes, as only initial positioning was necessary at the start of each pass.

The corresponding numerical simulations were performed using QForm UK 11.0.2 in explicit mode. The simulation model included the forging block, two flat dies identical to the real forging press, and a virtual manipulator for workpiece positioning. Tetrahedral finite elements were used in combination with an adaptive meshing strategy, resulting in up to 117,000 elements in highly deformed regions. The plastic material behavior was described using the experimentally determined flow curves obtained from the DRX investigations, while additional temperature-dependent material properties were taken from literature [28]. This includes thermal conductivity, density, elastic modulus and specific heat capacity. The dies were modeled as rigid bodies at 400 °C, with a die–workpiece heat transfer coefficient of 30,000 W/m²K and a Coulomb friction coefficient of 0.3. Heat exchange with the environment was considered using an ambient temperature of 20 °C and an air–workpiece heat transfer coefficient of 30 W/m²K. Adaptive meshing was employed to ensure sufficient resolution in highly deformed regions. The extended damage model, as described by Eq. 3-

14, was implemented via a Lua-based user subroutine, which received stress, temperature, and damage-related state variables from the FE simulation at each time increment and computed the corresponding damage evolution.

Fig. 5 presents the results of the validation forging experiments. In addition to the experimental forging results, the figure also includes the corresponding simulation results obtained using the extended damage model (Fig. 5, bottom).

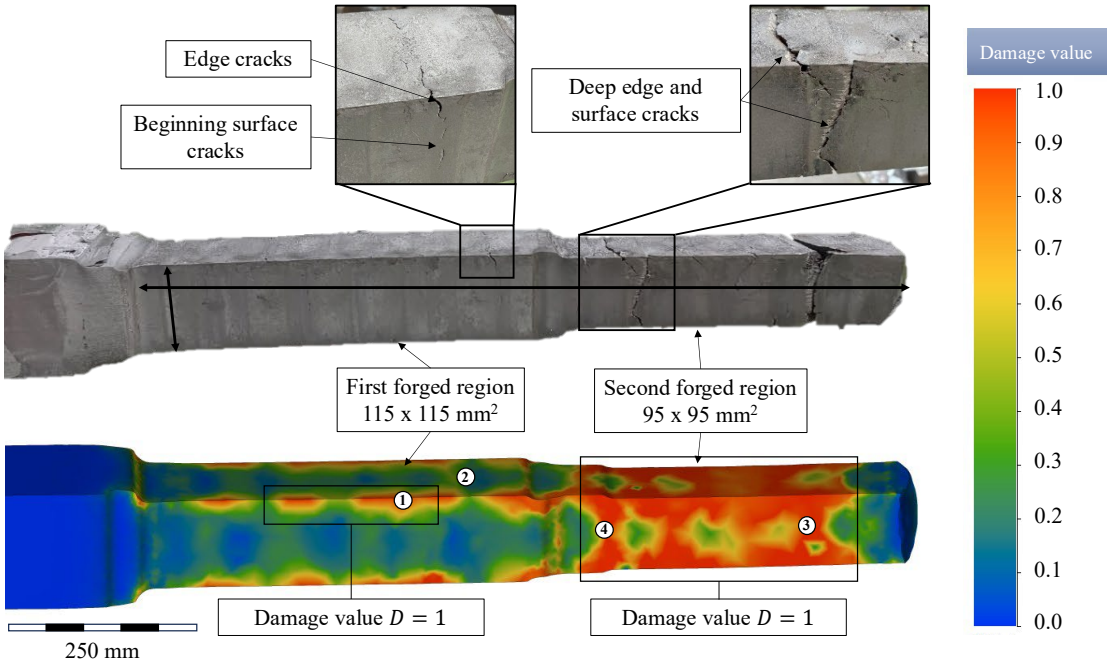

Fig. 5. Experimental and simulation validation. Top: Result of the forging experiment with crack visualization. Bottom: Simulation result with damage model.

The demonstrator component exhibits two clearly distinguishable damage regions in which pronounced cracking was intentionally induced. In the first forged region with the larger cross-section (115 × 115 mm²), clear edge cracks and locally initiated surface cracks are observed. In contrast, the second forged region with the smaller cross-section (95 × 95 mm²) shows extensive surface and edge cracking with significantly greater crack depth.

The numerical results demonstrate that the extended damage model is capable of reproducing the dominant damage mechanisms observed during the forging process. In the first step region, the simulation predicts distinct damage maxima at the workpiece edges, which correspond to the experimentally observed crack locations (Fig. 5, marking 1). However, the model does not fully capture the initiation of isolated surface cracks in this region, as the calculated damage values remain below the critical threshold of $D = 1$ (Fig. 5, marking 2). This deviation is likely caused by small variations in the manual positioning of the initial forging stroke, which may result in an unintended overlap of die edges in subsequent strokes and thereby promote localized damage accumulation not represented in the idealized simulation setup. In the second forged region, the damage model predicts critical damage values of $D = 1$ over large areas of the side surfaces and edges of the workpiece, which is confirmed by the occurrence of cracks in the experimental trials (Fig. 5, marking 3). Furthermore, the simulation reveals a damage zone extending from the transition between the second and first step toward the workpiece center and head. This arrow-shaped damage zone is reflected in the experimental forging results by diagonally oriented surface cracks (Fig. 5, marking 4).

Conclusion and Outlook

This work presented an extended damage modeling framework tailored to the specific conditions of open-die forging. Building on the Lemaitre damage model, the formulation was enhanced to include the effects of dynamic and static recrystallization, thereby capturing essential microstructural

mechanisms influencing damage accumulation and healing at elevated temperatures. The incremental nature of the process and the presence of dwell times were explicitly addressed.

The required material parameters were identified through a comprehensive experimental program. Hot tensile tests conducted at multiple temperatures were used to determine the parameters of the base Lemaitre damage model. The dynamic recrystallization behavior was characterized by hot compression tests performed at different temperatures and strain rates, while static recrystallization kinetics were derived from stress relaxation experiments carried out over a relevant temperature range. The effect of static recrystallization on damage evolution was further investigated by combining tensile and compression tests with detailed metallographic analyses. These investigations demonstrated that static recrystallization has a pronounced healing effect on existing damage: a nearly complete static recrystallization resulted in a reduction of the void area fraction by approximately 25.6 %, clearly confirming the damage-mitigating capability of recrystallization processes.

The damage model was implemented into a finite element framework and validated by open-die forging experiments on a demonstrator component. The simulations showed good agreement with experimentally observed damage and crack locations, confirming the model's ability to capture critical damage zones and characteristic damage patterns under industrially relevant conditions.

Future work will focus on examining the constitutive description of SRX-induced damage healing in more detail by means of dedicated numerical case studies and corresponding experiments, in order to explicitly validate the proposed SRX–damage coupling. Furthermore, the influence of individual process parameters on material damage during open-die forging will be systematically investigated. By analyzing the effects of parameters such as forging temperature, height reduction, bite ratio, dwell time, and tool geometry, critical process conditions can be identified. This will enable the development of damage-minimized forging strategies and support the reliable processing of demanding alloys, ultimately contributing to improved component quality and reduced scrap rates.

References

[1] H. Zhang, H. Tu, C. Yuan, Y. Li, X. Chen, H. Wang, Predicting forging defects using FEM: a brief review, Int J Adv Manuf Technol 141 (2025) 1143–1157.

[2] W.A. Knight, Simplified early cost estimating for hot-forged parts, Int J Adv Manuf Technol 7 (1992) 159–167.

[3] L. Niu, Q. Zhang, Y. Zhang, J. Wang, W. Luo, D. Liu, T. Ma, X. Velay, Study on Near-Net Shape Forging of Large Marine Crank Throws, Metals 15 (2025) 14.

[4] D. Marini, J.R. Corney, Process selection methodology for near net shape manufacturing, Int J Adv Manuf Technol 106 (2020) 1967–1987.

[5] P. Brozzo, B. Deluca, R. Rendina, A new method for the prediction of formability limits in metal sheets, Proceedings of the 7th Biennial Conference (1972).

[6] P.-O. Bouchard, L. Bourgeon, S. Fayolle, K. Mocellin, An enhanced Lemaitre model formulation for materials processing damage computation, Int J Mater Form 4 (2011) 299–315.

[7] M. Bambach, M. Imran, Extended Gurson–Tvergaard–Needleman model for damage modeling and control in hot forming, CIRP Annals 68 (2019) 249–252.

[8] J. Lemaitre, How to use damage mechanics, Nuclear Engineering and Design 80 (1984) 233–245.

[9] G. Rüf, C. Sommitsch, B. Buchmayr, On the interaction of ductile damage and materials softening of a Ni-base alloy during hot deformation, International Journal of Materials Research 98 (2007) 1146–1155.

[10] X. Li, C. Liebsch, G. Hirt, J. Lohmar, Modelling of void healing in hot rolling due to recrystallization, Prod. Eng. Res. Devel. 14 (2020) 43–52.

[11] A.E. Tekkaya, P.-O. Bouchard, S. Bruschi, C.C. Tasan, Damage in metal forming, CIRP Annals 69 (2020) 600–623.

[12] A.K. Ghosh, A Criterion for ductile fracture in sheets under biaxial loading, Metall Trans A 7 (1976) 523–533.

[13] D. Zhao, J. Bandstra, H. Kuhn, A New Fracture Criterion for Fracture Prediction in Metalworking Processes, Concurrent engineering approach to materials processing (1992) 107–119.

[14] P. Christiansen, C.V. Nielsen, P.A. Martins, N. Bay, Predicting the onset of cracks in bulk metal forming by ductile damage criteria, Procedia Engineering 207 (2017) 2048–2053.

[15] M. Kukuryk, Analysis of the coupling thermo-mechanical and crack model for the FEM simulation of the multi-stage forging process of die steel, Author(s) (2019), p. 20034.

[16] X. Shang, Z. Cui, M.W. Fu, A ductile fracture model considering stress state and Zener–Hollomon parameter for hot deformation of metallic materials, International Journal of Mechanical Sciences 144 (2018) 800–812.

[17] P.F. Gao, J. Guo, M. Zhan, Z.N. Lei, M.W. Fu, Microstructure and damage based constitutive modelling of hot deformation of titanium alloys, Journal of Alloys and Compounds 831 (2020) 154851.

[18] J. Lemaitre, A Course on Damage Mechanics, Springer Berlin / Heidelberg, Berlin, Heidelberg (1996).

[19] J. Humphreys, G.S. Rohrer, and A. Rollett, Recrystallization and Related Annealing Phenomena, Elsevier Science, London (2014).

[20] M. Sun, L. Hao, S. Li, D. Li, Y. Li, Modeling flow stress constitutive behavior of SA508-3 steel for nuclear reactor pressure vessels, Journal of Nuclear Materials 418 (2011) 269–280.

[21] H. Brüggemann, S. Sasaki, M. Röder, T. Katsumura, D. Bailly, Characterization and Modelling of Microstructure Evolution and Flow Stress of Single-Phase Austenite and Ferrite Phases in Duplex Stainless Steels, Metals 15 (2025) 130.

[22] L.P. Karjalainen, Stress relaxation method for investigation of softening kinetics in hot deformed steels, Materials Science and Technology 11 (1995) 557–565.

[23] G. Gottstein, Physical Foundations of Materials Science, Springer Berlin Heidelberg, Berlin, Heidelberg (2004).

[24] R.K. Abu Al-Rub, G.Z. Voyiadjis, On the coupling of anisotropic damage and plasticity models for ductile materials, International Journal of Solids and Structures 40 (2003) 2611–2643.

[25] A. Heiser, J. Gerlach, D. Bailly, G. Hirt, Investigation of the Influence of Static Recrystallization on Void Evolution After Hot Compression Forming, in: T. Bauernhansl, A. Verl, M. Liewald, and H.-C. Möhring, (Eds.), Production at the Leading Edge of Technology, Springer Nature Switzerland, Cham (2024), pp. 335–344.

[26] DIN EN ISO 6892-1:2020-06, Metallic materials - Tensile testing - Part 1: Method of test at room temperature (ISO 6892-1:2019); German version EN ISO 6892-1:2019.

[27] DIN EN 10228-4:2016-10, Non-destructive testing of steel forgings - Part 4: Ultrasonic testing of austenitic and austenitic-ferritic stainless steel forgings; German version EN 10228-4:2016.

[28] M. Spittel, T. Spittel, Steel symbol/number: X165CrMoV12/1.2601, in: W. Martienssen and H. Warlimont, (Eds.), Metal Forming Data of Ferrous Alloys - deformation behaviour, Springer Berlin Heidelberg, Berlin, Heidelberg (2009), pp. 480–485.

The publication of this article was funded by the RWTH Aachen University 10.13039/501100007210